



# Undulation enables gliding in flying snakes

Isaac J. Yeaton<sup>1,4</sup>✉, Shane D. Ross<sup>2</sup>, Grant A. Baumgardner<sup>1</sup> and John J. Socha<sup>3</sup>

**When flying snakes glide, they use aerial undulation. To determine if aerial undulation is a flight control strategy or a non-functional behavioural vestige of lateral undulation, we measured snake glides using high-speed motion capture and developed a new dynamical model of gliding. Reconstructions of the snake's wing-body reveal that aerial undulation is composed of horizontal and vertical waves, whose phases differ by 90° and whose frequencies differ by a factor of two. Using these results, we developed a three-dimensional mathematical model of snake flight that incorporates aerodynamic and inertial effects. Although simulated glides without undulation attained some horizontal distance, they are biologically unrealistic because they failed due to roll and pitch instabilities. In contrast, the inclusion of undulation stabilized the rotational motion and markedly increased glide performance. This work demonstrates that aerial undulation in snakes serves a different function than known uses of undulation in other animals, and suggests a new template of control for dynamic flying robots.**

Undulation is an evolutionarily ancient locomotor pattern used by many long-bodied animals for propulsion in fluids and in terrestrial environments. Animals use environment-dependent patterns of axial bending that enable the body to push against the surrounding medium in a stable and efficient manner<sup>1,2</sup>. Common wave patterns include lateral undulation on flat and rough surfaces<sup>3–6</sup>, sidewinding on sand<sup>7,8</sup>, viscous swimming at low Reynolds number<sup>9–11</sup> and inertial swimming at high Reynolds numbers<sup>12–15</sup>. In contrast to the well understood role of aquatic and terrestrial undulation, the role of aerial undulation in limbless flyers is unknown.

Flying snakes (*Chrysopelea*) are the only known limbless vertebrates capable of flight<sup>16</sup>. When gliding, these animals use aerial undulation, moving horizontally downward through the air by converting gravitational potential energy into kinetic energy, producing aerodynamic lift and drag (Supplementary Videos 1–4). Their undulation is characterized by an S-shape body planform (Fig. 1), a low undulation frequency of 1–2 Hz, and a flattened, aerofoil-like body cross-section<sup>17–21</sup>. Most glides begin with a jump, during which a wave of dorsoventral flattening passes from the head to the vent<sup>22</sup>. This flattening transforms the snake's circular cross-section into a roughly triangular aerofoil, with favourable aerodynamic properties and gentle stall characteristics<sup>23–25</sup>.

Aerial undulation continuously reconfigures the snake's body, transforming the animal into a morphing wing (Fig. 1e). Previous studies of snake glides determined that flying snakes always undulate while airborne. However, it is unclear if undulation is a functional requirement of gliding, or simply a behavioural remnant of snake locomotion, as all snakes are capable of lateral undulation, an evolutionary ancient motor pattern produced by waves of muscle contraction propagating down the body<sup>26</sup>. Some non-flying snakes react to dropping by undulating (J.J.S., personal observation). Previous measurements of aerial undulation under-resolved the animal's body, making it difficult to quantify the time-varying body configuration. This lack of resolution has previously limited our ability to test how aerial undulation affects flight dynamics and reveal the mechanical function of aerial undulation<sup>17,19,20</sup>.

From analogy with terrestrial and aquatic undulation, one might expect that aerial undulation generates propulsive thrust. On solid

media, undulatory locomotion occurs due to distributed contact forces over ventral and lateral regions of the body, and in water, the fluid displacement or suction along the body causes forward motion<sup>27</sup>. In both cases, the net propulsive thrust acts predominantly within the plane of undulation. Modulation of the body out of plane (in the vertical direction) may be used for secondary purposes, such as reducing drag or increasing the normal force<sup>4,8</sup>. Forward motion stops when undulation stops, and because of the body's distributed contact area and neutral buoyancy, rotational stability is not a primary concern.

For flying snakes, a successful glide requires generation of aerodynamic forces to offset the animal's weight. Lift and drag forces are produced by air flowing over the flattened body as it accelerates downward under gravity, with the reciprocating motion produced by muscular contractions probably not enhancing force production<sup>19</sup>. The resulting aerodynamic forces should act out of the plane of undulation; furthermore, undulation should continuously change the distribution of forces on the body. As flying snakes have two additional rotational degrees of freedom (about the pitch and roll axes) compared with terrestrial undulators<sup>28</sup>, time-varying forces should affect the rotational behaviour<sup>29</sup>. These physical challenges of flight without wings, and the unique kinematics of flying snakes while airborne, suggest that aerial undulation does indeed have a functional role.

Here, we investigate the functional role of aerial undulation in snake gliding flight by assessing its effects on flight dynamics. Using high-speed motion capture and a large indoor glide arena, we quantify aerial undulation to provide an understanding of the entire morphing wing-body. This higher-fidelity understanding of the body enables us to develop an anatomically accurate theoretical model of snake flight, which we combine with previous aerodynamic force measurements to test the performance and stability properties of aerial undulation in limbless flight. Our results provide a foundation for designing snake-inspired robots that use aerial undulation to glide through the air, adding to the growing library of robotic snake locomotion.

**Flying snakes use waves of orthogonal bending when gliding**  
Aerial undulation consists of coupled waves of horizontal and vertical bending. We used high-speed motion capture to record the position of 11–17 landmarks placed along the body from seven

<sup>1</sup>Department of Mechanical Engineering, Virginia Tech, Blacksburg, VA, USA. <sup>2</sup>Department of Aerospace and Ocean Engineering, Virginia Tech, Blacksburg, VA, USA. <sup>3</sup>Department of Biomedical Engineering and Mechanics, Virginia Tech, Blacksburg, VA, USA. <sup>4</sup>Present address: Johns Hopkins University Applied Physics Laboratory, Laurel, MD, USA. ✉e-mail: [Isaac.Yeaton@jhuapl.edu](mailto:Isaac.Yeaton@jhuapl.edu)

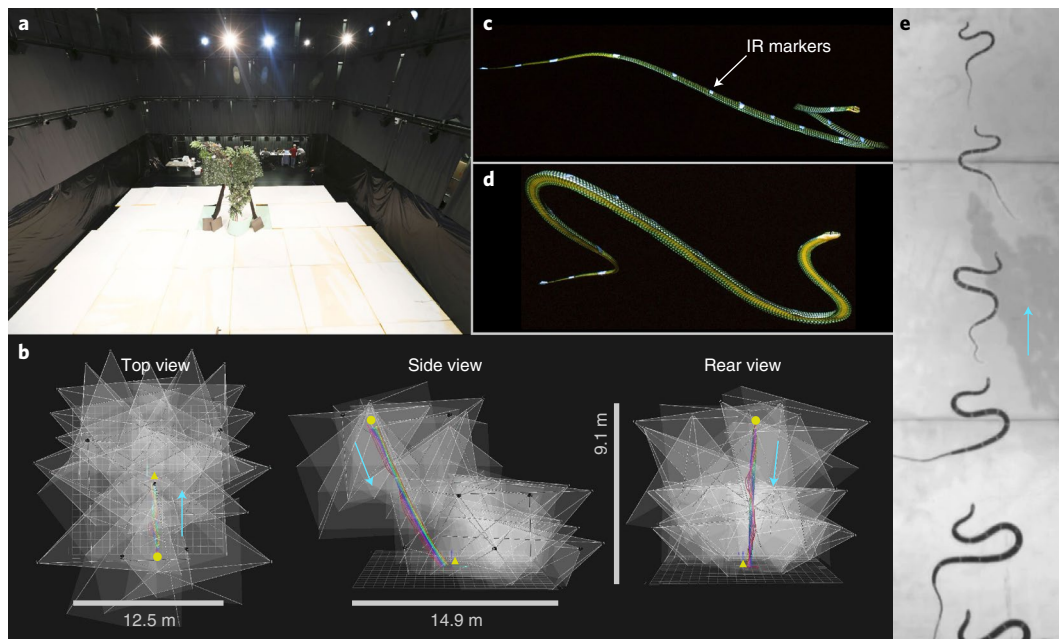


**Fig. 1 | Measurements of gliding in flying snakes.** **a**, Front view of the glide arena from the top of the launch platform. The floor was covered with white foam padding and a tree placed in the centre to encourage glides. Motion-capture cameras were placed around the perimeter. **b**, Top, side and rear views of the glide arena, with infrared-camera field-of-view cones overlaid. The arrow denotes the direction of the glide from the start (yellow circle) to the end (yellow triangle); individual infrared marker trajectories (one colour per marker) for one glide are overlaid. **c**, The flying snake, *Chrysopelea paradisi*, in the mid-glide posture, with a flattened body and infrared (IR) markers placed along the dorsal surface and tail. The anterior body shows the characteristic out-of-plane twisting at the U-bends due to the vertical body wave. **d**, Ventral view of a *C. paradisi* gliding with a relatively open body shape. See Supplementary Figs. 1 and 2 for additional photographs of mid-air body configurations. **e**, Morphing wing-body seen from snapshots of an overhead view of aerial undulation. Motion is from bottom to top, with the snake appearing smaller as it moves away from the camera (Supplementary Video 4). This is the same trajectory as shown in **b**. Relative to leaving contact with the launch branch, timestamps for each snapshot are 0.486 s, 0.572 s, 0.688 s, 0.856 s, 1.066 s and 1.296 s. The snake contacts the ground at 1.440 s. Credit: **a**, Michael Diersing.

snakes gliding from a height of 8.3 m in an indoor glide arena (Fig. 1 and Supplementary Videos 4 and 5). We used spline fits to the landmark points on the body in 36 trials to create a continuous and three-dimensionally accurate representation of the snake,  $\mathbf{r}$  (Supplementary Video 6). Using the unit tangent vector,  $\hat{\mathbf{t}} = \partial\mathbf{r}/\partial s$ , we decompose the complex motion of aerial undulation into two bending angle waves that travel down the body (Fig. 2). The horizontal and vertical waves are given by

$$\bar{\theta}(s, t) = -\tan^{-1} \hat{t}_x / \hat{t}_y \quad \text{and} \quad \bar{\psi}(s, t) = \sin^{-1} \hat{t}_z \quad (1)$$

where  $\bar{\theta}(s, t)$  and  $\bar{\psi}(s, t)$  are local angles the body makes relative to the horizontal and vertical directions, respectively, as functions of arc length  $s$  and time  $t$ .

Our data reveal that flying snakes employ two waves: a large-amplitude horizontal wave and a newly discovered smaller-amplitude vertical wave, both of which travel down the body from the head to the vent in a consistent manner (Fig. 2 and Supplementary Video 5). These waves form after an initial transient as the snake jumps into a relatively straight posture and then forms the characteristic S-shape glide posture.

There are four features of aerial undulation relating the vertical wave to the horizontal wave (Fig. 2a). First, the vertical wave has spatial and temporal frequencies twice those of the horizontal wave, indicating that the body has twice as many vertical bends as lateral bends (Fig. 2a,e). Second, the U-bends on the flying snake's body can be identified as the zero crossings on the bending-angle plot (Fig. 2b). Third, these zero crossings are maxima of the vertical wave, indicating that the horizontal and vertical waves are phase-shifted by  $90^\circ$ . Fourth, the maximum out-of-plane bending

occurs at the U-bends and roughly halfway along the straight segments. At the U-bends, the snake's aerofoil cross-section twists due to the body's out-of-plane motion (Fig. 1c,d).

The instantaneous shape of the travelling waves varies with time as the animal accelerates and produces aerodynamic forces, but several features remain common (Fig. 2). The horizontal wave is a flat-topped sinusoid whose amplitude,  $80\text{--}120^\circ$ , depends on the number of spatial periods, with fewer spatial periods resulting in higher horizontal bending angles. The vertical wave is a narrow-peaked sinusoid with broad troughs, with amplitudes ranging from  $20^\circ$  to  $45^\circ$ .

We quantified the wave's spatial and temporal characteristics using complex orthogonal decomposition, decomposing the bending-angle data into time-varying modal shapes<sup>30,31</sup> (Supplementary Information). Flying snakes use horizontal wave shapes with 1–1.5 spatial periods that undulate at 1–1.7 Hz, and vertical wave shapes with 2–3 spatial periods that undulate at 2–3.4 Hz. The vertical-to-horizontal frequency ratios are close to two: the spatial and temporal frequency ratios are  $1.87 \pm 0.35$  and  $1.98 \pm 0.21$ , respectively.

There is an additional component to aerial undulation that we term 'dorsoventral bending', which is the up-and-down motion of the posterior body relative to the head. We quantified dorsoventral bending as the slope of a linear regression of the vertical bending angles, with values ranging from  $-20^\circ$  to  $30^\circ$ . Dorsoventral bending was always present in recorded glides, but was not significantly related to the number of spatial periods (Wald test with  $t$  distribution).

### A new mathematical model of limbless flight

We tested the effects of coupled horizontal and vertical waves and dorsoventral bending on glide dynamics using a new, anatomically

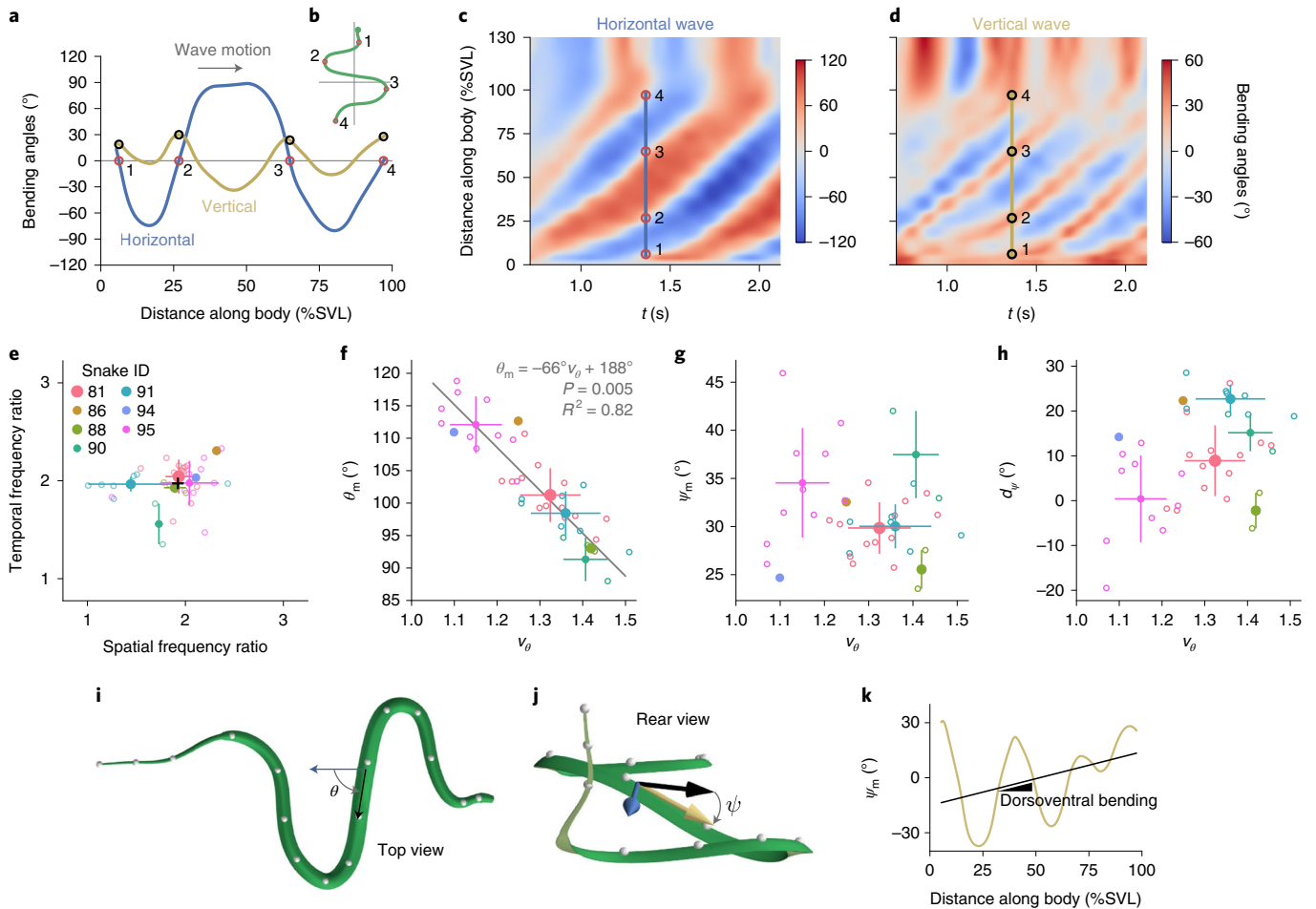


**Fig. 2 | Measured body kinematics in flying snakes.** **a, b**, Horizontal and vertical bending angles versus snout-vent length (SVL) (**a**) with an overhead view of the snake’s backbone (**b**) about halfway through a glide. **c, d**, Space-time bending plots showing the travelling waves of bending. The time-point indicated in **a** and **b** is denoted by the vertical lines. Numbered points in **a–d** denote zero crossings of the horizontal wave, corresponding to peaks in the vertical wave, indicating maximum out-of-plane bending at the U-bends. **e–h**, Summary of waveform characteristics. Colours indicate different snakes; small open markers indicate unique glides and solid markers indicate individual averages. The size of the solid marker denotes the snake’s relative mass. Error bars indicate 1 s.d. (some may be smaller than the marker size). **e**, Ratios of temporal and spatial frequencies of the horizontal and vertical waves. The black + is the overall average. **f**, The average horizontal wave amplitude is inversely proportional to the number of horizontal spatial periods. The grey linear regression line relating  $\theta_m$  to  $\nu_\theta$  is  $\theta_m = -66^\circ \nu_\theta + 188^\circ$ . See text for details. **g**, Average vertical wave amplitude versus number of spatial periods of the horizontal wave. **h**, Average dorsoventral bending angle (out-of-plane gross body bending) versus number of spatial periods of the horizontal wave. **i**, Top view of the snake showing the definition of the horizontal bending angle,  $\theta$ , as the angle between the blue unit vector in the  $-\hat{y}$  direction and the projection of the yellow tangent vector into the horizontal plane (black vector). **j**, Rear view of the snake showing the definition of the vertical bending angle,  $\psi$ , as the angle between the yellow tangent vector and the horizontal projection. On the snake images, dark green is the dorsal surface, yellow-green is the ventral surface and grey are the infrared marker locations. **k**,  $d_\psi$  is quantified as the slope of the best-fit line to the average vertical wave amplitude (yellow) as a function of distance along the body. An example dorsoventral bending calculation is shown in black for one snake.

accurate model of snake flight. Manipulation of the model allows us to systematically test how the components of aerial undulation (horizontal wave amplitude, number of spatial periods and undulation frequency) affect short-term and long-term glide dynamics.

We prescribe travelling waves that capture the observed kinematic features of the measured bending waves (Fig. 2a) by defining the ‘aerial serpenoid curve’. The horizontal wave is modelled as a large-amplitude, flat-topped sinusoid, and the vertical wave as a small-amplitude sinusoid, parameterized as

$$\bar{\theta}(s, t) = \theta_m \sin \left[ \frac{\pi}{2} \cos \left( \frac{2\pi\nu_\theta}{L} s - 2\pi f_\theta t + \phi_\theta \right) \right] \quad (2)$$

$$\bar{\psi}(s, t) = \psi_m \cos \left( \frac{2\pi\nu_\psi}{L} s - 2\pi f_\psi t + \phi_\psi \right) + \frac{d_\psi}{L} s \quad (3)$$

where  $\theta_m$  and  $\psi_m$  are the maximum horizontal and vertical bending angles,  $\nu$  is the number of spatial periods,  $f$  is the undulation frequency,  $\phi$  is the phase shift,  $d_\psi$  is the dorsoventral bending angle and  $L$  is the snout-vent length (see Fig. 2f,g). The horizontal and vertical waves are coupled as in the kinematic data, with  $\nu_\psi = 2\nu_\theta$ ,  $f_\psi = 2f_\theta$  and  $\phi_\psi = 2(\phi_\theta - \pi/2)$  (Fig. 2e), reducing the kinematic model to five variables that define the body shape:  $\theta_m$ ,  $\psi_m$ ,  $\nu_\theta$ ,  $f_\theta$  and  $d_\psi$ . The position  $\mathbf{r} = [x, y, z]$  of the body relative to the centre of mass is calculated by integrating the serpenoid curve as  $\partial_s x = \cos \bar{\psi} \sin \bar{\theta}$ ,  $\partial_s y = -\cos \bar{\psi} \cos \bar{\theta}$  and  $\partial_s z = \sin \bar{\psi}$ .

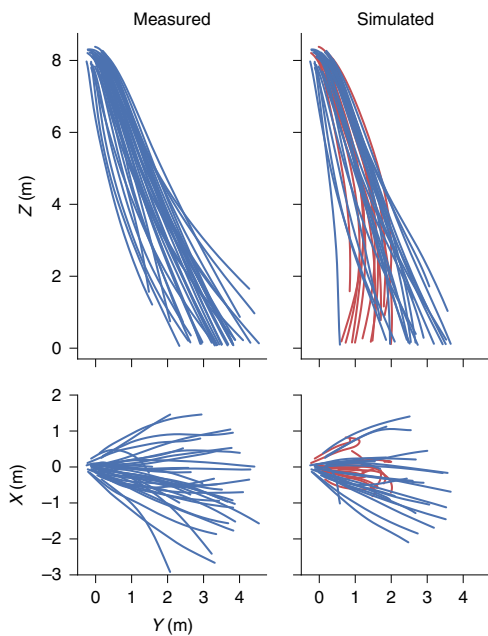


**Fig. 3 | Comparison of measured and simulated snake glides.** Side ( $Z$  versus  $Y$ ) and top ( $X$  versus  $Y$ ) views of the centre of mass for experimentally measured (left) and simulated (right) glides for each of the 36 trials analysed. The coordinate system is the same as in Fig. 1. Simulated glides that did not shallow are denoted in red. The average body kinematics (Fig. 2f–h) of the measured glides, as well as the individual snake’s snout-vent length and mass, were used to define the aerial serpenoid curve for the simulations; measured glide initial position and velocity defined the simulations’ initial conditions. The measured glides show slightly better performance than simulated glides, but they show qualitatively similar behaviour. All measured glides shallowed; simulated glides that did not are affected by a pitch instability discussed later.

The centre-of-mass position,  $\mathbf{R}_0$ , and body orientation (yaw, pitch and roll angles) are found by integrating the translational and rotational equations of motion,

$$\int_0^L (\mathbf{f}_L + \mathbf{f}_D) ds - m\mathbf{g} = m\ddot{\mathbf{R}}_0 \quad (4)$$

$$\mathbf{M}_A = \underbrace{\mathbf{I}_0 \cdot \dot{\boldsymbol{\omega}} + \boldsymbol{\omega} \times (\mathbf{I}_0 \cdot \boldsymbol{\omega})}_{\text{rigid-body terms}} + \underbrace{[\dot{\mathbf{I}}_0] \cdot \boldsymbol{\omega} + \boldsymbol{\omega} \times \mathbf{h}_0 + [\dot{\mathbf{h}}_0]}_{\text{inertial moments}} \quad (5)$$

where  $\mathbf{f}_L$  and  $\mathbf{f}_D$  are infinitesimal lift and drag forces calculated from the local velocity using previously measured quasi-steady lift and drag coefficients<sup>33</sup>, and simple sweep theory to account for curved segments<sup>29,32</sup>;  $\mathbf{M}_A$  is the aerodynamic moment and  $m$  is the animal mass (for other variables, see Methods). Because the snake continuously reconfigures its body, the non-aerodynamic contributions to rotational motion are decomposed into rigid-body terms and variable-geometry inertial moments.

To validate that the mathematical model gives physically realistic results, we simulated glides using aerial serpenoid curve parameters, snake masses and lengths, and glide initial conditions derived from our measurements. Fig. 3 compares the measured and simulated glides. The range of the simulated glides captures the qualitative features of the measured glides. The horizontal distance travelled and lateral spread in landing location of simulated glides is slightly less, but the simulated glides usually shallow and are similarly steep. Some of the simulated trajectories (in red) curve backwards, which

does not occur with real snakes. This difference is due to a pitch instability, and is discussed later. These results indicate that the undulating, but uncontrolled, snake model gives similar behaviour to observed glides, but that the model requires further refinement to capture all features of the observed glides.

### Undulation enhances rotational stability thereby increasing glide performance

To test the effects of aerial undulation on glide performance, we simulated glides with  $f_\theta = 0$  Hz (no undulation) and  $f_\theta = 1.2$  Hz (the observed mean frequency), while varying  $\nu_\theta$  and  $\theta_m$  (Fig. 4a). On the basis of the range observed from the kinematic data, we discretized the shape space into 121 shapes, with  $1 \leq \nu_\theta \leq 1.5$  body waves and horizontal wave amplitudes  $90^\circ \leq \theta_m \leq 119^\circ$ . We further segregated the shape space along the diagonal of observed shapes (Fig. 4b). The lower left portion contains visibly ‘open’ shapes and the upper right visibly ‘closed’ shapes. The vertical wave amplitude and the dorsoventral bending angle were kept constant at  $20^\circ$  and  $10^\circ$ , respectively. Their combined effect is tested later. We simulated glides until the snake’s centre of mass contacted the ground or until any of the orientation angles became unstable by exceeding a threshold of  $85^\circ$  (ref. 29). If any angle exceeded the threshold, we deemed the glide to be unstable. We tested short-term glide dynamics with a launch height of 10 m, and long-term glide dynamics with a launch height of 75 m, both with and without undulation. The 10-m height is consistent with this and other experimental studies<sup>18</sup>, and the 75-m height was based on the height of dipterocarp trees in the snake’s native Indo-Malayan forest habitat<sup>33</sup>.

The model shows that aerial undulation produces positive effects on glide performance, generally increasing the horizontal and vertical distances travelled before the simulated snake becomes unstable (Fig. 4, Supplementary Table 1 and Video 7). For short glides with launch heights of 10 m, 94% of glides with undulation were stable, whereas only 50% of glides without undulation were stable. Among the observed body shapes, all glides with undulation were stable, whereas only 35% of glides without undulation were stable. The effect of undulation on increasing the horizontal glide distance is less pronounced, with the average distance increasing from 4 m to 4.3 m. Considering only the experimentally observed shapes, the average glide distance increases to 4.9 m.

Undulation has a larger effect during long glides starting from 75 m (Fig. 4 and Supplementary Table 1). Undulation increased both the horizontal and vertical distances travelled before becoming unstable in 86% of glides. For observed shapes with undulation, all glides covered greater vertical distance, and 92% of glides travelled farther. The glides without undulation that travelled farther only did so by an average of 0.16 m. Conversely, undulation increased the average horizontal distance travelled by 6.9 m.

### Dorsoventral bending controls pitching motion

To elucidate the effects of the vertical wave amplitude and dorsoventral bending on glide dynamics, we varied these parameters over the observed experimental range (Fig. 2). We simulated glides with  $\psi_m = 0^\circ$ ,  $10^\circ$  and  $20^\circ$  (planar undulation to increasing levels of out-of-plane motion) and dorsoventral bending of  $-20^\circ$  to  $20^\circ$  in  $10^\circ$  increments (Fig. 5a), for 11 different body shapes along the best-fit line (Fig. 2f).

Vertical wave variations have a small effect on the glide trajectory (Supplementary Information), whereas dorsoventral bending exhibits a larger effect. A perfectly planar snake ( $\psi_m = 0^\circ$ ), never observed in the experimental glide trials, performed worst. Increasing the vertical wave amplitude increased glide performance, due to the out-of-plane twisting of the cross-section to a more advantageous angle of attack for force production (Fig. 2j).

In contrast to the vertical wave amplitude, dorsoventral bending had a marked effect on glide performance by affecting the pitch

dynamics (Fig. 5). At  $d_{\psi} = -20^{\circ}$ , with the posterior body beneath the head, the glides did not shallow, but instead became unstable in pitch before falling 10 m. At  $d_{\psi} = 20^{\circ}$ , with the posterior body above the head, the centre-of-mass trajectory curved backward, with some shapes landing behind the jump location. This poor glide performance is due to upward pitching of the body. Although the performance was poor, these glides were rotationally stable. At intermediate values of dorsoventral bending, all glides were stable, and performance was best at  $d_{\psi} = 10^{\circ}$ , where the pitch angle is closest to the starting value near  $0^{\circ}$ . The trends in pitching dynamics as dorsoventral bending is varied are robust to changes in the aerodynamic force coefficients, showing the same trends even when the lift-to-drag ratio is doubled (Supplementary Information).

To understand the coupling of dorsoventral bending, pitching motion and glide performance, we also simulated glides with the rotational equations of motion disabled. Instead of solving the coupled nonlinear system of equations (4) and (5), we sampled the aerodynamic forces on the body at different phases through the undulation cycle and integrated equation (4) to calculate the centre-of-mass position and speed. At each phase of undulation, we calculated the resulting moments acting on the body by evaluating equation (5), with the orientation kept constant. In effect, this manipulation is a ‘virtual wind tunnel’ experiment, in which the dynamic model is used to calculate the distributed forces acting on the body as it accelerates. This technique allows us to remove the coupling of the translational and rotational motion to quantify the separate aerodynamic and inertial contributions to the rotational motion. We report the phase-averaged pitch moment at the end of a simulated glide, where speeds are greatest and forces are largest.

As dorsoventral bending increases from  $-20^{\circ}$  to  $10^{\circ}$ , the landing position of the simulated snake increases as the average pitch moment increases toward zero (Fig. 5d). At a dorsoventral bending of  $20^{\circ}$ , the phase-averaged pitch moment becomes positive, and glide performance decreases. For each dorsoventral bending angle, the glide performance and average pitch moment also depend on the shape used, specifically the number of spatial periods and the horizontal wave amplitude. For a given shape, dorsoventral bending has a large effect on the average pitch moment, and as the number of spatial periods increases the moments diverge, becoming more positive or negative depending on  $d_{\psi}$ . Large negative pitch moments are associated with  $d_{\psi}$  of  $-20^{\circ}$  to  $0^{\circ}$ , near-zero pitch moments for  $d_{\psi} = 10^{\circ}$  and large positive pitch moments for  $d_{\psi} = 20^{\circ}$ . The sign of the phase-averaged pitch moments in Fig. 5e corresponds to the pitching up or pitching down seen in Fig. 5c and the resulting glide performance in Fig. 5b. Fig. 5f highlights how the average pitch moment is smallest for shapes with fewer spatial periods (and higher horizontal wave amplitudes). The point of zero pitch moment varies for each shape, but occurs for a positive dorsoventral bending angle.

The slope provides a measure of the sensitivity of a particular shape to changes in pitch moment due to changes in dorsoventral bending during a glide. Shapes in the lower right of the wave-shape space are more sensitive to the out-of-plane motion of the body, whereas shapes in the upper left are less affected.

Our parametric study of vertical wave amplitude and dorsoventral bending provides insight into the observed flying snake kinematics, and also points to a pitch control strategy for a flying-snake-inspired robot. The vertical wave causes the body to twist out of plane, modifying the local orientation of the flattened aerofoil with the free-stream airflow. Dorsoventral bending controls the magnitude and sign of the aerodynamic pitch moment that acts on the body. Net non-zero pitch moments were associated with the snake becoming unstable in pitch and/or overall poor glide performance. A flying snake can control the pitch moment by mid-flight variations of the dorsoventral bending angle or the horizontal wave shape. Correcting a pitch instability requires a change of the sign of the pitch moment (Fig. 5f), which only occurs as dorsoventral bending changes.

The model results suggest a pitch control strategy that involves varying the dorsoventral bending (moving the posterior body above or below the head) in a time-varying manner to change the net pitch moment acting on the animal or robot. Because the pitch moment is sensitive to dorsoventral bending, a semi-periodic change in dorsoventral bending should be able to correct for any inherent pitch instability or disturbance during a glide. The time-varying motion of the posterior body up and down is seen in footage of flying snakes, and is probably constrained by the zygapophyses, which are bony protrusions from the vertebra that limit dorsiflexion<sup>34</sup>.

In the mathematical formulation of flying snake kinematics, equation (3), dorsoventral bending has the same form as a steering parameter in planar snake-inspired robots<sup>35</sup>, where the horizontal wave is biased laterally, changing the distribution of forces and causing the robot to move in circular arcs. In flying snakes, a bias is present in the vertical wave, not the horizontal wave. Its use for steering is uncertain, but our results demonstrate clearly that the bias controls rotational stability by modifying the aerodynamic force distribution.

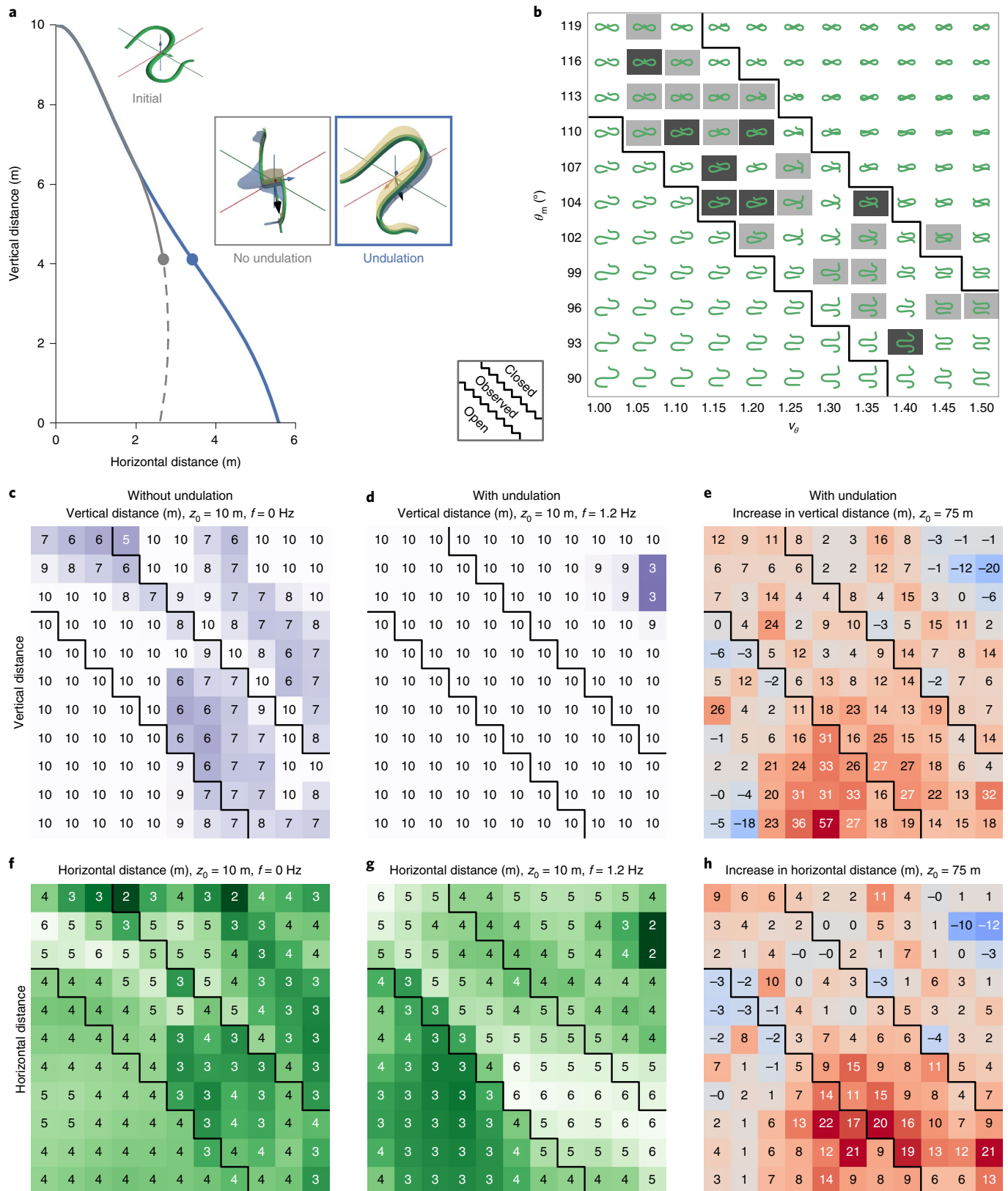
### Inertial manoeuvring in flying snakes

The phase-averaging analysis enables us to quantify the relative contributions of aerodynamic and inertial moments to glide dynamics (Fig. 6). From the rotational equations of motion (5), the orientation of the body is affected by both aerodynamic forces and the changing mass distribution. The aerodynamic contribution (Fig. 6a) increases with time as the velocity increases, whereas the inertial contribution (Fig. 6b) stays constant. Both moments are periodic, with only the pitch moment showing a non-zero phase average.

**Fig. 4 | Simulated flying snake glides.** **a**, Simulated glide trajectories with (blue) and without (grey) undulation. Snapshots of body orientation at the same height, denoted by the filled markers, are shown, with the lift (blue) and drag (yellow) forces overlaid. The dashed line indicates the extrapolated landing location of the grey trajectory. The glide without undulation becomes unstable before reaching the ground, whereas the glide with undulation does not. Supplementary Video 7 depicts both glides in detail. **b**, Horizontal-wave-shape space used for simulated glides. Grey and black boxes indicate histogram counts (one or two, respectively) of experimentally observed body shapes (that is, a two-dimensional histogram of Fig. 2f). The shape space is demarcated into regions (inset) of experimentally observed shapes in the middle diagonal, and non-observed shapes in the two corners, classified as open in the lower left and closed in the upper right. **c–h**, Performance summary of glide simulations. Axis labels and shape regions are the same as in **b**. **c, f**, Cases without undulation ( $f = 0$  Hz). **d, e, g, h**, Cases with undulation ( $f = 1.2$  Hz). Columns 1 and 2 depict short-glide performance (initial height  $z_0 = 10$  m), where lighter and darker colours indicate better and poorer performance, respectively. Column 3 depicts long glides beginning from  $z_0 = 75$  m, where darker red indicates better performance with undulation and darker blue indicates better performance without undulation. All simulations were for a snake with snout-vent length of 70 cm and mass of 38 g. **c**, Vertical distance travelled during short glides of  $z_0 = 10$  m before becoming unstable with no undulation. ‘10’ denotes a stable glide, and many shapes within the observed region are unstable. **d**, Vertical distance travelled during short glides before becoming unstable with undulation. Undulation improves the stability properties of shapes within the observed region. **e**, Increase in vertical distance due to undulation for long glides beginning at  $z_0 = 75$  m. Glides with undulation perform better. **f**, Horizontal glide distance without undulation. **g**, Horizontal glide distance with undulation. Undulation generally increases the glide distance, especially within the observed region. **h**, Increase in horizontal glide distance due to undulation for long glides. Glides with undulation perform better.

We calculate the inertial-to-aerodynamic moment ratio via the peak-to-peak amplitudes from the respective time series (Fig. 6c) about the orientation angles for various  $d_{wp}$  and  $\nu_\theta$ . About the pitch and roll axes, inertial moments initially dominate, but within one undulation cycle their contribution rapidly decreases. Inertial yaw

moments are generally an order of magnitude greater than aerodynamic yaw moments and greater than inertial moments about the other axes. Inertial yaw moments arise from the large-amplitude horizontal wave and the broad S-shape of flying snakes. This result suggests that flying snakes could employ inertial yaw turning as a



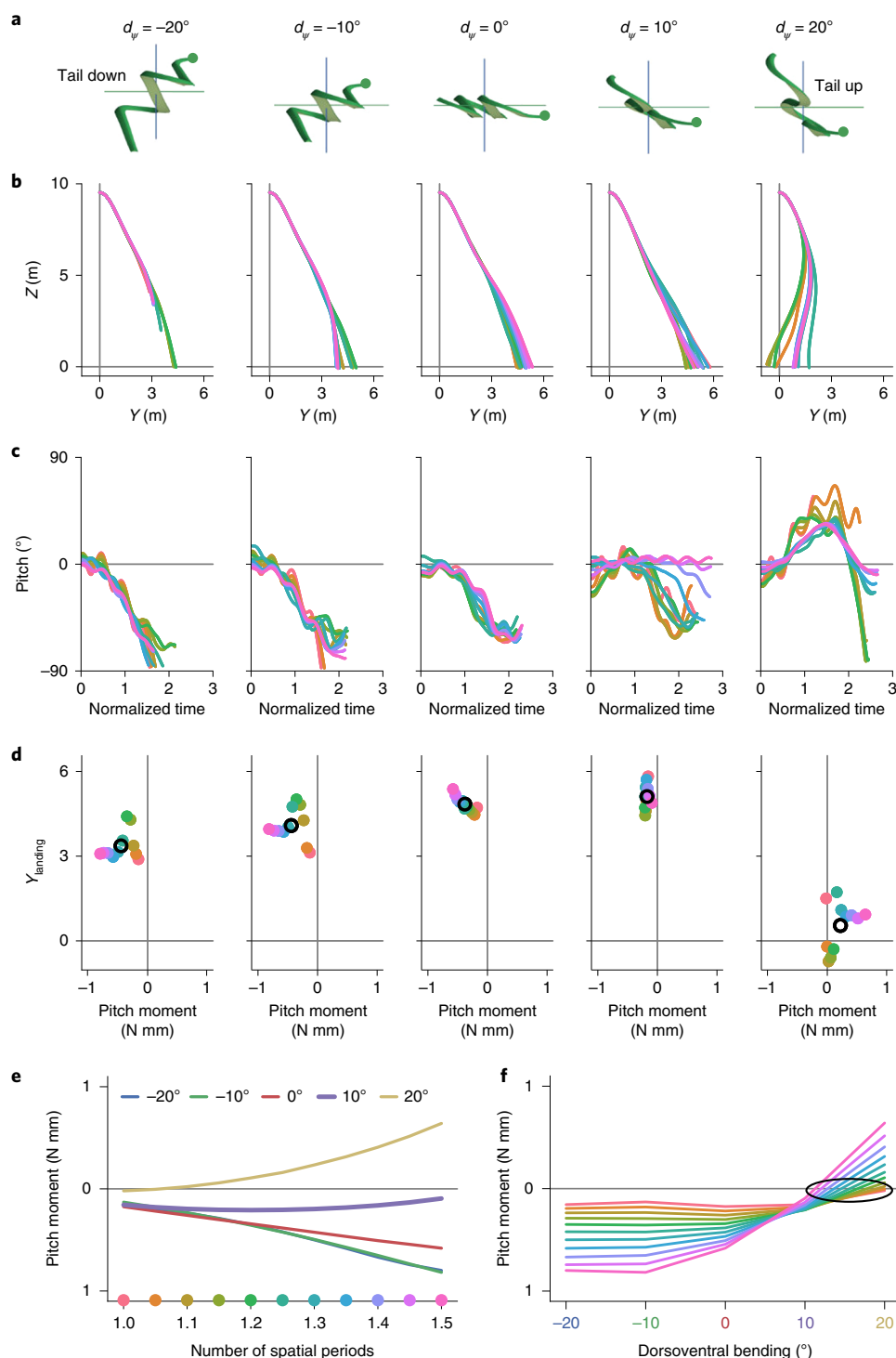


**Fig. 5 | Effect of dorsoventral bending ( $d_\psi$ ) on glide dynamics and control of pitching motion.** In all panels, solid thin grey lines indicate positions and/or angles at zero. **a**, Side views of simulated snake kinematics, where motion would be from left to right, for  $d_\psi$  ranging from  $-20^\circ$  to  $20^\circ$  and  $\psi_m = 20^\circ$  (the same as for glides in Fig. 4). The head of the snake is indicated with the green circle, and the dorsal and ventral surfaces are indicated in dark green and yellow-green, respectively. Negative  $d_\psi$  causes the posterior body to fall below the head (tail down); both negative and positive values are seen in snake glides. **b**, Side view of the centre-of-mass trajectory, where colours indicate different  $\nu_\theta$  and  $\theta_m$  combinations (see **e** for the colour key). The performance peaks at  $d_\psi = 10^\circ$  and is worst at  $d_\psi = 20^\circ$ . The stability is worst for  $-20^\circ$ , as some glides do not reach the ground. **c**, Pitch angle versus normalized time (physical time multiplied by the undulation frequency). Most glides pitch down, especially for negative dorsoventral bending. Best-performing glides occur for  $d_\psi = 10^\circ$ , where the pitch angle is near zero. **d**, Terminal landing position versus phase-averaged pitch moment for different dorsoventral bending angles and numbers of spatial periods. The black open circle denotes the average. **e**, Effect of the number of spatial periods and dorsoventral bending on the phase-averaged pitch moment. Different-coloured lines indicate different  $d_\psi$  combinations, while coloured points indicate different  $\nu_\theta$  and  $\theta_m$  combinations along the regression line of Fig. 2f. The sign of the pitch moment depends on the dorsoventral bending angle, while the magnitude depends on the number of spatial periods. **f**, Alternative view of **e**, where lines indicate different  $\nu_\theta$  and  $\theta_m$  combinations. The point of zero pitch moment occurs for positive  $d_\psi$  and is indicated by the black oval. Varying  $d_\psi$  is more effective than varying  $\nu_\theta$  to change the sign and amplitude of the pitch moment.

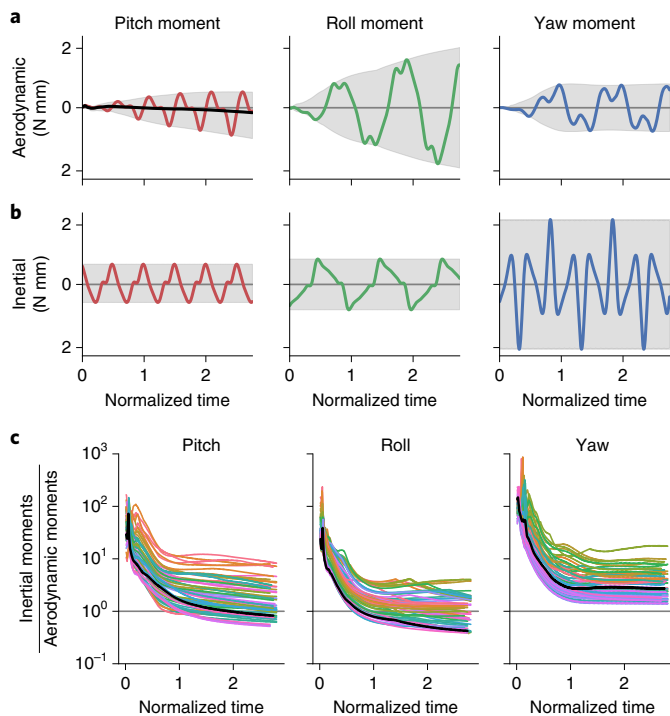


**Fig. 6 | Relative contributions of inertial and aerodynamic moments in the flying snake model.** **a**, Aerodynamic pitch, roll and yaw moments from the phase-averaging analysis (equation (5)). Periodic traces indicate the moment time series for one phase, while grey bands indicate the extrema for all phases. The magnitude increases with time because the speed increases as the simulated snake falls due to gravity. The black line is the phase-averaged pitch moment (used in Fig. 5d–f), which is non-zero. The phase-averaged roll and yaw moments are always zero. **b**, Inertial moments from the phase-averaging analysis. The extrema do not change with time because inertial moments are independent of the animal's speed. **c**, Relative contribution of inertial-to-aerodynamic moments (the peak-to-peak ratio of the moment time series) throughout a glide for different dorsoventral bending angles and numbers of spatial periods, with the vertical wave amplitude constant at  $20^\circ$ . Colours indicate different  $\nu_\theta$  combinations and are the same as in Fig. 5. The black line is the parameter combination of  $\nu_\theta$  and  $d_\psi$  shown in **a, b**. Inertial moments always dominate at the beginning of the glide. Inertial yaw moments always dominate, suggesting a mechanism of manoeuvring.

mechanism for manoeuvring. Such manoeuvres could be initiated by timing a bias to the horizontal wave during part of the undulation phase when inertial yaw moments are large.

### Implications for robotics

The newly discovered kinematic components of aerial undulation, particularly the coupled waves of bending, and their effects on flight dynamics, provide the theoretical basis for design of a bioinspired flying snake robot that glides using aerial undulation as a control template<sup>36</sup>. Such a robophysical model would allow for further investigation into the underlying biomechanical control mechanisms in flying snakes. Moreover, the aerial undulation template should markedly simplify the control of a flying-snake-like robot.

### Online content

Any methods, additional references, Nature Research reporting summaries, source data, extended data, supplementary information, acknowledgements, peer review information; details of author contributions and competing interests; and statements of

data and code availability are available at <https://doi.org/10.1038/s41567-020-0935-4>.

Received: 24 September 2018; Accepted: 11 May 2020;  
Published online: 29 June 2020

### References

- Walton, M., Jayne, B. C. & Bennet, A. F. The energetic cost of limbless locomotion. *Science* **249**, 524–527 (1990).
- Hopkins, J. K., Spranklin, B. W. & Gupta, S. K. A survey of snake-inspired robot designs. *Bioinspir. Biomim.* **4**, 021001 (2009).
- Guo, Z. V. & Mahadevan, L. Limbless undulatory propulsion on land. *Proc. Natl Acad. Sci. USA* **105**, 3179–3184 (2008).
- Hu, D. L., Nirody, J., Scott, T. & Shelley, M. J. The mechanics of slithering locomotion. *Proc. Natl Acad. Sci. USA* **106**, 10081–10085 (2009).
- Alben, S. Optimizing snake locomotion in the plane. *Proc. R. Soc. A* **469**, 20130236 (2013).
- Hirose, S. *Biologically Inspired Robots: Snake-like Locomotors and Manipulators* (Oxford University Press, 1993).
- Marvi, H. et al. Sidewinding with minimal slip: snake and robot ascent of sandy slopes. *Science* **346**, 224–229 (2014).
- Astley, H. C. et al. Modulation of orthogonal body waves enables high maneuverability in sidewinding locomotion. *Proc. Natl Acad. Sci. USA* **112**, 6200–6205 (2015).
- Pierce-Shimomura, J. T. et al. Genetic analysis of crawling and swimming locomotory patterns in *C. elegans*. *Proc. Natl Acad. Sci. USA* **105**, 20982–20987 (2008).
- Fang-Yen, C. et al. Biomechanical analysis of gait adaptation in the nematode *Caenorhabditis elegans*. *Proc. Natl Acad. Sci. USA* **107**, 20323–20328 (2010).
- Hums, I. et al. Regulation of two motor patterns enables the gradual adjustment of locomotion strategy in *Caenorhabditis elegans*. *eLife* **5**, e14116 (2016).
- Taylor, S. G. Analysis of the swimming of long and narrow animals. *Proc. R. Soc. A* **214**, 158–183 (1952).
- Gazzola, M., Argentina, M. & Mahadevan, L. Gait and speed selection in slender inertial swimmers. *Proc. Natl Acad. Sci. USA* **112**, 3874–3879 (2015).
- Ijspeert, A. J. Central pattern generators for locomotion control in animals and robots: a review. *Neural Netw.* **21**, 642–653 (2008).
- Ijspeert, A. J., Crespi, A., Ryczko, D. & Cabelguen, J.-M. From swimming to walking with a salamander robot driven by a spinal cord model. *Science* **315**, 1416–1420 (2007).
- Socha, J. J., Jafari, F., Munk, Y. & Byrnes, G. How animals glide: from trajectory to morphology. *Can. J. Zool.* **93**, 901–924 (2015).
- Socha, J. J. Gliding flight in the paradise tree snake. *Nature* **418**, 603–604 (2002).
- Socha, J. J., O'Dempsey, T. & LaBarbera, M. A 3-D kinematic analysis of gliding in a flying snake, *Chrysopelea paradisi*. *J. Exp. Biol.* **208**, 1817–1833 (2005).
- Socha, J. J. & LaBarbera, M. Effects of size and behavior on aerial performance of two species of flying snakes (*Chrysopelea*). *J. Exp. Biol.* **208**, 1835–1847 (2005).
- Socha, J. J., Miklasz, K., Jafari, F. & Vlachos, P. P. Non-equilibrium trajectory dynamics and the kinematics of gliding in a flying snake. *Bioinspir. Biomim.* **5**, 045002 (2010).
- Socha, J. J. Gliding flight in *Chrysopelea*: turning a snake into a wing. *Integr. Comp. Biol.* **51**, 969–982 (2011).
- Socha, J. J. Becoming airborne without legs: the kinematics of take-off in a flying snake, *Chrysopelea paradisi*. *J. Exp. Biol.* **209**, 3358–3369 (2006).
- Holden, D., Socha, J. J., Cardwell, N. D. & Vlachos, P. P. Aerodynamics of the flying snake *Chrysopelea paradisi*: how a bluff body cross-sectional shape contributes to gliding performance. *J. Exp. Biol.* **217**, 382–394 (2014).
- Krishnan, A., Socha, J. J., Vlachos, P. P. & Barba, L. A. Lift and wakes of flying snakes. *Phys. Fluids* **26**, 031901 (2014).
- Miklasz, K., LaBarbera, M., Chen, X. & Socha, J. J. Effects of body cross-sectional shape on flying snake aerodynamics. *Exp. Mech.* **50**, 1335–1348 (2010).
- Lillywhite, H. B. *How Snakes Work: Structure, Function and Behavior of the World's Snakes* (Oxford University Press, 2014).
- Gemmell, B. J., Colin, S. P., Costello, J. H. & Dabiri, J. O. Suction-based propulsion as a basis for efficient animal swimming. *Nat. Commun.* **6**, 8790 (2015).
- Dudley, R. Mechanisms and implications of animal flight maneuverability. *Integr. Comp. Biol.* **42**, 135–140 (2002).
- Jafari, F., Tahmasian, S., Ross, S. D. & Socha, J. J. Control of gliding in a flying snake-inspired *n*-chain model. *Bioinspir. Biomim.* **12**, 066002 (2017).
- Feeny, B. F. & Feeny, A. K. Complex modal analysis of the swimming motion of a whiting. *J. Vib. Acoust.* **135**, 021004 (2013).

31. Feeny, B. F., Sternberg, P. W., Cronin, C. J. & Coppola, C. A. Complex orthogonal decomposition applied to nematode posturing. *J. Comput. Nonlinear Dyn.* **8**, 041010 (2013).
32. Ellington, C. P. The aerodynamics of hovering insect flight. I. The quasi-steady analysis. *Philos. Trans. R. Soc. B* **305**, 1–15 (1984).
33. Dudley, R. & DeVries, P. Tropical rain forest structure and the geographical distribution of gliding vertebrates. *Biotropica* **22**, 432–434 (1990).
34. Moon, B. R. Testing an inference of function from structure: snake vertebrae do the twist. *J. Morphol.* **241**, 217–225 (1999).
35. Saito, M., Fukaya, M. & Iwasaki, T. Modeling, analysis, and synthesis of serpentine locomotion with a multilink robotic snake. *IEEE Control Syst. Mag.* **22**, 64–81 (2002).
36. Full, R. J. & Koditschek, D. E. Templates and anchors: neuromechanical hypotheses of legged locomotion on land. *J. Exp. Biol.* **202**, 3325–3332 (1999).

**Publisher's note** Springer Nature remains neutral with regard to jurisdictional claims in published maps and institutional affiliations.

© The Author(s), under exclusive licence to Springer Nature Limited 2020

## Methods

**Experimental design.** The objective of this study was to determine the effect of aerial undulation on glide performance in flying snakes. We first measured the kinematics of aerial undulation in live flying snakes (*Chrysopelea paradisi*) using high-speed motion capture. For each snake, we placed infrared reflective markers along the dorsal surface of the body such that its aerial flattening was not affected, and then recorded the marker positions as snakes glided through a large indoor arena. In post-processing, we fitted splines to the marker locations, which were then used to quantify aerial undulation with high fidelity (Supplementary Videos 5 and 6). The experimentally measured kinematics then served as input to a mathematical model of snake flight. We systematically varied the model parameters to test how different body configurations affected flight dynamics and stability.

**Snake gliding experiments.** Glides from the paradise tree snake, *C. paradisi* (seven individuals, mass 37.3–107.2 g, length 63–88 cm) were recorded in a large indoor arena in the Moss Arts Center at Virginia Tech. Trials were conducted in The Cube, a four-storey black-box theatre, modified to meet Virginia Tech Animal Care and Use Protocol Committee requirements. The facility is 9.1 m high, 12.5 m wide, and 14.9 m long. To prevent the snakes from landing on three perimeter walkways, black plastic sheeting was hung along the sides and back wall and curtains were pulled over the walkway railing. To prevent injury upon landing, the floor was covered with sheets of 5-cm soft foam padding (Super Soft Foam, Foam Factory, flat sheets of 2" × 82" × 76"). An artificial tree covered with fake leaves and vines was placed in the centre of the glide arena to encourage jumps and a consistent landing location. A scissor lift was used to raise the snakes to a height of 8.3 m for jumps and glides. The scissor lift was draped with black cloth to prevent the snakes from contacting the lift mechanism. A branch from an oak tree was used as a launch branch from which the snakes jumped.

A 23-camera motion-capture system (Oqus 500, Qualisys) was used to record the infrared markers placed on the snake's dorsal surface, using a frame rate of 179 frames s<sup>-1</sup>. Three cameras were placed along the top of the glide arena to record the initial portion of the glide trajectory. The other 20 cameras were placed along the walkway railings. The motion-capture system was calibrated at the start of each testing day. Calibrations were done by removing one foam sheet and placing an inertial coordinate system marker on the floor. Next, a calibration wand was used to 'paint' the measurement volume that approximated the glide path of the snakes. This procedure started at the top of the scissor lift, and moved downward to the arena floor.

Two visible-light high-speed cameras (APX-RS, Photron; 500 frames s<sup>-1</sup>) were placed on the ceiling of the glide arena. One camera was positioned directly above the launch branch and the other halfway between the launch branch and the landing tree. Two other cameras were also used: one (4K, Sony) was placed orthogonal to the launch branch to record the jump, and a second (TS3, Fastec) was placed 2 m above the ground to record late-phase gliding and landing.

Glide trials were conducted over nine consecutive days in May 2015. Snakes were transported from their animal care facility to The Cube in reptile bags placed in a heated cooler. Snakes were then transferred to an incubator heated to 33 °C. The temperature of the glide arena was set to 26–28 °C. Between 11 and 17 infrared-reflective tape markers (Vicon, approximately 1 × 1 cm<sup>2</sup> markers,  $\rho_{\text{tape}} = 0.02 \text{ g cm}^{-2}$ ) were placed along the dorsal surface. A marker was placed at the top of the head, the vent and the tip of the tail. Depending on the size and length of the animal, two or three markers were placed along the tail, and the remaining markers distributed along the body. To ensure that the tape did not affect the snake's flattening, the skin was stretched ventrally and tape placed over the ribs, but not contacting the ventral scale. Missing tape markers were replaced at the start of each day of testing.

Snakes were transported in reptile bags from the incubator to the scissor lift and brought to a height of approximately 8.3 m. The height from the tip of the launch branch to the foam floor was measured with a laser range finder (Bosch, GLM 50, ±1.6-mm accuracy). The cameras and motion-capture system were then set to record, and the snake removed from the reptile bag and placed on the launch branch. All glides originated with a volitional jump from the launch branch. Gentle prodding was used if the animal did not immediately jump. Once the animal jumped and glided to the ground, an assistant would capture the animal, rebag it and place it back in the incubator. The camera and motion-capture systems were then manually triggered and the data transferred to a computer. Snakes were allowed to rest for at least 15 min between glides.

At the end of each day of recording, an overhead image was taken of each snake next to a calibration target. The snake's backbone in these images was digitized manually and used to measure the length between markers<sup>37</sup>.

**Three-dimensional data processing.** A total of 131 glides were recorded, and for each trial the raw landmark points were labelled and exported using Qualisys Track Manager software. On the basis of data quality (number of missing markers, length of time markers were missing), 36 trials from seven animals were selected for further processing. For each trial, time series were truncated to start and end times when no markers were missing. Gaps of recorded marker locations were filled separately for each marker using an unscented Kalman filter with Rauch-Tung-Striebel smoothing<sup>38,39</sup>. The filter provides smoothed estimates of the  $[x, y, z]$

positions of the marker, while also incorporating estimates of the velocities and accelerations. Although the filter estimates smoothed position values for the entire trajectory, only the gap regions for each individual marker trajectory were filled.

To remove noise from the marker position time series, a forward-backward second-order Butterworth filter was applied. The optimal filter cutoff frequencies were found separately for each marker's  $[x, y, z]$  time series. This approach gives equal weight to both signal distortion and noise passed through the filter<sup>40</sup>. The technique involves fitting linear regressions of the  $L^2$ -norm residual error with respect to frequency at high cutoff frequencies until the  $R^2$  value of the linear fit drops below 0.95. The  $y$  intercept of the linear regression defines the noise floor; the frequency at which a horizontal line from the  $y$  intercept intersects the residual curve defines the optimal cutoff frequency.

Splines were used to reconstruct the snake's backbone position, given as  $\mathbf{r}(s, t) = [x(s, t), y(s, t), z(s, t)]$ . At each time step, a global natural cubic spline was fitted to the filtered positions<sup>41</sup>. The spline is evaluated with the measured arc-length coordinate,  $s$ . Overhead videos of gliding (Supplementary Video 4) indicate that the snake has a neck region directly behind the head that does not bend. We model this region by constraining the spline with a virtual marker placed directly behind the head and halfway between the head and second marker on the body. The direction behind the head was determined from the inertial velocity of the head marker, as the neck region and head move together as the snake undulates.

We define bending waves from the angle data, as opposed to the position data, because periodic angle changes more closely resemble the underlying muscle activation pattern known to produce undulation in snakes<sup>42,43</sup>, enabling more accurate kinematic modelling<sup>9</sup>.

We quantified the spatiotemporal characteristics of aerial undulation using complex orthogonal decomposition<sup>30,31</sup> separately on the horizontal and vertical waves, with the linear fit to the vertical wave removed. Complex orthogonal decomposition decomposes oscillatory motion into time-varying modal shapes. The modes are ranked by the amount of explained variance, with only a few modes needed to describe the wave. The spatial mode encodes the spatial frequency and the modal activity encodes the undulation frequency. The spatial mode and modal activity are both complex functions with real and imaginary components. The spatial and temporal frequencies are calculated as the number of revolutions the modes make in the complex plane.

The horizontal wave is more organized than the vertical wave, with only one or two modes required to describe 95% of the observed variance, and the first mode accounting for 88% of the variance. The vertical wave requires four modes to explain 95% of the variance, with the first mode contributing only 66% of the variance (Supplementary Information).

**Statistical analysis of complex orthogonal decomposition results.** The statistical results, shown in Fig. 2 and discussed in the text, describing the relationships between number of spatial periods, horizontal wave amplitude, vertical wave amplitude and dorsoventral bending, were calculated using a linear regression from `scipy.stats.linregress`. The  $P$  value returned from `linregress` is a two-sided  $P$  value assuming the null hypothesis that the slope is zero. Internally, the method uses a Wald test, assuming a  $t$  distribution for the test statistic.

**Theoretical model of snake flight.** To test the effect of horizontal and vertical waves of bending on snake flight dynamics, we formulated a new theoretical model of snake gliding. This anatomically accurate model complements previous reduced-order models of snake gliding<sup>44,45</sup> and more recent kinematic chain models<sup>29</sup>. The model consists of three components: the kinematic equations of motion, the equations of motion and the aerodynamic force model. We define the body kinematics in a local co-moving frame that is centred at the centre of mass. We define how the body moves in this frame using the aerial serpenoid equations presented in the main text. The co-moving frame then translates and rotates under the translational and rotational equations of motion subject to gravity, aerodynamic forces, and inertial forces due to the prescribed undulation.

For the angles describing the orientation of the co-moving frame, we use the standard aircraft angle convention: positive pitch indicates nose tipping up, positive roll indicates banking to the right, and positive yaw indicates rotating left about the vertical axis.

For completeness of the full description of the kinematic and dynamic models presented below, we repeat portions of the mathematical modelling section from the main text.

**Kinematic model.** We model the instantaneous body posture relative to a centre-of-mass frame with the aerial serpenoid curve, a compound space curve with travelling waves of horizontal and vertical bending. We modify the standard serpenoid curve used for modelling snake-like locomotion<sup>6,35</sup> to better approximate a flat-topped horizontal wave. The horizontal and vertical bending waves are

$$\bar{\theta}(s, t) = \theta_m \sin \left[ \frac{\pi}{2} \cos \left( \frac{2\pi\nu_{\theta}}{L} s - 2\pi f_{\theta} t + \phi_{\theta} \right) \right] \quad (6)$$

$$\bar{\psi}(s, t) = \psi_m \cos \left( \frac{2\pi\nu_{\psi}}{L} s - 2\pi f_{\psi} t + \phi_{\psi} \right) + \frac{d_{\psi}}{L} s \quad (7)$$

where  $s$  is in metres. The lateral and vertical waves are coupled, reducing the kinematic model to five variables to define the body shape:  $\theta_m, \psi_m, \nu_\theta, f_\theta$  and  $d_\psi, \phi_\theta$  is used to minimize the initial inertial moments on the body (discussed below), but is not a shape parameter.

The position of the body in the co-moving frame satisfies  $\partial_s x = \cos \bar{\psi} \sin \bar{\theta}$ ,  $\partial_s y = -\cos \bar{\psi} \cos \bar{\theta}$ ,  $\partial_s z = \sin \bar{\psi}$ . When the horizontal and vertical waves are prescribed, the instantaneous body position in the co-moving frame is found by integration,

$$\begin{aligned} x(s, t) &= \int_0^s \cos \bar{\psi} \sin \bar{\theta} ds' \\ y(s, t) &= \int_0^s -\cos \bar{\psi} \cos \bar{\theta} ds' \\ z(s, t) &= \int_0^s \sin \bar{\psi} ds' \\ \mathbf{r}(s, t) &= [x(s, t), y(s, t), z(s, t)] \end{aligned} \quad (8)$$

where  $\mathbf{r}$  is the position of an infinitesimal element of the snake, and the sign convention is such that the head points in the  $+y$  direction, the right flank is in the  $+x$  direction and the dorsal surface is in the  $+z$  direction. The velocity,  $[\dot{\mathbf{r}}]$ , and acceleration,  $[\ddot{\mathbf{r}}]$ , of the body are found from fourth-order accurate finite differences, as the position is not defined analytically.

The anterior body kinematics are modified to meet the experimental observation that the head orientation remains relatively fixed compared with the rest of the body, a characteristic property of gaze stabilization<sup>46</sup>. We modify the first 7.5% of the lateral and vertical waves such that they are linear functions, which results in the head and neck of the snake being oriented in the forward direction (the head points in the  $+y$  direction<sup>47</sup>). We match the angles at the end of the neck region for both the horizontal and vertical wave,

$$c_{\theta, \text{neck}} = \frac{\theta(s_{\text{neck}}, t)}{s_{\text{neck}}} \quad (9)$$

$$c_{\psi, \text{neck}} = \frac{\psi(s_{\text{neck}}, t)}{s_{\text{neck}}} \quad (10)$$

and the horizontal and vertical waves in the neck region become

$$\theta(0 \leq s \leq s_{\text{neck}}) = s c_{\theta, \text{neck}} \quad (11)$$

$$\psi(0 \leq s \leq s_{\text{neck}}) = s c_{\psi, \text{neck}} \quad (12)$$

**Aerofoil coordinate system.** We model the flattened aerofoil orientation using the aerofoil coordinate system, which defines how the local airflow interacts with the body. The aerofoil coordinate system determines the ‘twist’ of the simulated snake body, accounting for the local twisting observed in the glide experiments. Unlike the travelling waves, we do not specify an explicit function for twist, but rather it varies passively with the local position of the body. The aerofoil coordinate system is defined by the local tangent direction

$$\hat{\mathbf{t}}(s, t) = \frac{\partial_s \mathbf{r}(s, t)}{\|\partial_s \mathbf{r}(s, t)\|} \quad (13)$$

and the co-moving frame vertical  $\hat{\mathbf{z}} = [0, 0, 1]$  direction. We take the width as the chord-line direction and constrain it to reside in the horizontal plane of the co-moving frame. The chord-line direction,  $\hat{\mathbf{c}}$ , is defined as

$$\hat{\mathbf{c}} = \frac{\hat{\mathbf{z}} \times \hat{\mathbf{t}}}{\|\hat{\mathbf{z}} \times \hat{\mathbf{t}}\|} \quad (14)$$

and the backbone direction is defined as

$$\hat{\mathbf{b}} = \hat{\mathbf{t}} \times \hat{\mathbf{c}} \quad (15)$$

The local angle of attack is determined by the combination of the local chord-line direction and the co-moving frame orientation.

**Dynamic model.** The translational and rotational equations of motion are found using the Newton–Euler method,

$$\int_0^L (\mathbf{f}_L + \mathbf{f}_D) ds - m\mathbf{g} = m\ddot{\mathbf{R}}_0 \quad (16)$$

$$\mathbf{M}_A = \mathbf{I}_0 \cdot \dot{\boldsymbol{\omega}} + \boldsymbol{\omega} \times (\mathbf{I}_0 \cdot \boldsymbol{\omega}) + [\dot{\mathbf{I}}_0] \cdot \boldsymbol{\omega} + \boldsymbol{\omega} \times \mathbf{h}_0 + [\dot{\mathbf{h}}_0] \quad (17)$$

where each term is time varying, overdots denote inertial time derivatives, brackets denote co-moving frame time derivatives expressed in the inertial frame,  $\mathbf{g}$  is gravitational acceleration, and  $\mathbf{I}_0$  is the nine-component inertia dyadic. The angular velocity  $\boldsymbol{\omega}$  and centre-of mass velocity and position,  $\dot{\mathbf{R}}_0$  and  $\mathbf{R}_0$ , are solved

for numerically using a standard Dormand–Prince method. The aerodynamic moments are

$$\mathbf{M}_A = \int_0^L \mathbf{r} \times (\mathbf{f}_L + \mathbf{f}_D) ds \quad (18)$$

where  $\mathbf{f}_L$  and  $\mathbf{f}_D$  are the lift and drag force densities per unit length; the total lift and drag forces,  $\mathbf{F}_L$  and  $\mathbf{F}_D$ , are found by integrating the densities along the body. The angular momentum is

$$[\mathbf{h}_0] = \int_0^L \mathbf{r} \times \dot{\mathbf{r}} \rho(s) ds \quad (19)$$

and the angular momentum rate is

$$[\dot{\mathbf{h}}_0] = \int_0^L \mathbf{r} \times \ddot{\mathbf{r}} \rho(s) ds \quad (20)$$

where  $\rho(s)$  is the linear mass density.

**Co-moving frame orientation.** The kinematic differential equations complete the rotational equations of motion and are found by relating the change in comoving frame orientation (Euler angle rates) to the angular velocity as

$$\dot{\boldsymbol{\theta}} = \mathbf{K}^B \boldsymbol{\omega} = \mathbf{K} \mathbf{C} \boldsymbol{\omega} \quad (21)$$

where  ${}^B \boldsymbol{\omega}$  is the angular velocity expressed in the co-moving frame. Written in detail we have

$$\begin{bmatrix} \dot{\psi} \\ \dot{\theta} \\ \dot{\phi} \end{bmatrix} = \begin{bmatrix} -\sin \phi / \cos \theta & 0 & \cos \phi / \cos \theta \\ \cos \phi & 1 & \sin \phi \\ \sin \phi \tan \theta & \tan \theta & -\cos \phi \tan \theta \end{bmatrix} \begin{bmatrix} \omega_x \\ \omega_y \\ \omega_z \end{bmatrix}^B \quad (22)$$

See Supplementary Information for details.

**Aerodynamic lift and drag.** The lift and drag forces are the result of local fluid velocity, location along the body, and body orientation,

$$\begin{aligned} \mathbf{f}_L &= \frac{\rho U^2}{2} c(s) C_L(\alpha, Re) \hat{\mathbf{L}} \\ \mathbf{f}_D &= \frac{\rho U^2}{2} c(s) C_D(\alpha, Re) \hat{\mathbf{D}} \end{aligned} \quad (23)$$

and depend explicitly on the width  $c(s)$  of the animal (Supplementary Information). The lift and drag coefficients  $C_L(\alpha, Re)$  and  $C_D(\alpha, Re)$  are angle-of-attack and Reynolds number dependent and are taken from previous studies of flying snake aerodynamics<sup>23,24</sup>.

We use simple sweep theory to account for the non-perpendicular airflow interacting with the body. The aerodynamic force coefficients were measured for a section of the snake’s body perpendicular to the flow. However, the modelled snake has sections that are not perpendicular to the flow. To model these forces, we only use the component of the velocity that is perpendicular to the body, that is, the velocity component that resides in the  $\hat{\mathbf{c}}\text{--}\hat{\mathbf{b}}$  frame. We calculate the angle of attack and Reynolds number as

$$\alpha = \cos^{-1} \left( \frac{\hat{\mathbf{R}}_{CB} \cdot \hat{\mathbf{c}}}{U_\perp} \right) \quad \text{Re}(s, t) = \frac{\|\hat{\mathbf{R}}\| c(s)}{\nu} \quad (24)$$

where  $\hat{\mathbf{R}}_{CB}$  is the component of the inertial velocity  $\hat{\mathbf{R}} = \dot{\mathbf{R}}_0 + \boldsymbol{\omega} \times \mathbf{r} + [\underline{\mathbf{g}}]$  of a body element in the  $\hat{\mathbf{c}}\text{--}\hat{\mathbf{b}}$  plane, and  $\hat{\mathbf{c}}$  is the chord-line unit vector expressed in the inertial frame. The normal velocity is then  $U_\perp = \|\hat{\mathbf{R}}_{CB}\|$ .

The lift and drag unit vectors,  $\hat{\mathbf{L}}$  and  $\hat{\mathbf{D}}$ , are calculated such that the drag force acts along the perpendicular velocity and lift acts normal to the perpendicular velocity. That is,

$$\hat{\mathbf{D}} = -\hat{\mathbf{R}}_{CB} / U_\perp \quad \hat{\mathbf{L}} = \hat{\mathbf{t}} \times \hat{\mathbf{D}} \quad (25)$$

Using the above expression, the drag vector will always point in the correct direction, but the lift vector can be flipped by 180° about  $\hat{\mathbf{D}}$ . We account for this by checking in which quadrant around the cross-section the velocity vector is located, and then modifying the sign of the angle of attack and orientation of the unit lift vector as

$$\alpha, \hat{\mathbf{L}} = \begin{cases} \alpha, \hat{\mathbf{L}} & \text{if } \alpha_c > 90^\circ \text{ and } \alpha_b \geq 90^\circ \\ -\alpha_c, \hat{\mathbf{L}} & \text{if } \alpha_c > 90^\circ \text{ and } \alpha_b > 90^\circ \\ \alpha_c - 180^\circ, -\hat{\mathbf{L}} & \text{if } \alpha_c \geq 90^\circ \text{ and } \alpha_b > 90^\circ \\ 180^\circ - \alpha_c, -\hat{\mathbf{L}} & \text{if } \alpha_c \geq 90^\circ \text{ and } \alpha_b \geq 90^\circ \end{cases} \quad (26)$$

where  $\alpha_c$  and  $\alpha_b$  are the angles between the perpendicular velocity  $\hat{\mathbf{R}}_{CB}$  and the  $\hat{\mathbf{c}}$  and  $\hat{\mathbf{b}}$  directions, respectively.

**Complete dynamic model.** The complete model consists of specifying the body kinematics using equations (6), (7) and (8) by selecting  $\nu_\theta$ ,  $\theta_m$ ,  $\psi_m$ ,  $f_\theta$  and  $d_\psi$ . With the kinematics specified, the equations of motion (4) and (5) and kinematic differential equations (22) are integrated, with external aerodynamic forces given by equation (23). The rotationally invariant model consists of the above, except that equation (5) is not integrated and the force and moment histories are recorded.

**Glide simulations.** Glides were simulated by integrating the equations of motion forward in time using a fifth-order accurate Dormand–Prince method until the centre of mass contacted the ground with  $R_{0,z} < 0$ .

**Simulation initial conditions.** The kinematics model, equations (6) and (7), requires specification of  $\nu$ ,  $f$  and  $\phi$ . The number of body waves and undulation frequency are set from the parameter space observed in our experiments.

$\phi_0$  plays an important role because of the high inertial torques on the body about the yaw axis (Fig. 6b,c), especially at the beginning of the glide when aerodynamic forces are small. We therefore bias the undulation at the start of each glide to minimize this effect. This biasing is done by setting the phase shift to minimize the  $L^2$ -norm of the angular momentum expressed in the co-moving frame

$$\|[\mathbf{h}_0]\| = \left\| \int_0^L \mathbf{r} \times \dot{\mathbf{r}} \rho(s) ds \right\| \quad (27)$$

A non-zero angular momentum would cause the simulated snake to rotate in place. For planar undulation, the angular momentum only has a  $z$  component, so it is always possible to find an initial phase shift such that the angular momentum is zero. This norm is not guaranteed to be zero when the vertical wave is incorporated, as the vertical wave moves angular momentum into the other two axes.

The equations of motion require initial conditions, including the jump height, velocity, angular velocity, and yaw, pitch and roll Euler angles. The height and horizontal velocity were set to  $z_0 = 10$  m and  $v_{x0} = 1.7$  m s<sup>-1</sup>, respectively, on the basis of initial jump velocities measured previously<sup>18</sup>. The angular velocity was set to zero, such that the yaw, pitch and roll rates are zero. The initial Euler angles were found such that average angle deviations were zero. The initial angles were found by simulating one undulation cycle of the snake with gravity and aerodynamic forces turned off. The initial yaw, pitch and roll angles are found as the negative of the average of each Euler angle time series.

**Reporting Summary.** Further information on research design is available in the Nature Research Reporting Summary linked to this article.

### Data availability

All data that support the plots within this paper and other findings of this study are available in the Data subdirectories of the code repository and at <https://drive.google.com/drive/folders/1FpSBUD1XY3guuWjGUE5V7dqluNkoXyKy> for processed experiment and simulation data.

### Code availability

Code used to analyse the glide trials and perform the glide simulations is available at [github.com/TheSochaLab/Undulation-enables-gliding-in-flying-snakes](https://github.com/TheSochaLab/Undulation-enables-gliding-in-flying-snakes).

### References

37. Astley, H. C., Astley, V. E., Brothers, D. & Mendelson, J. R. III Digital analysis of photographs for snake length measurement. *Herpetol. Rev.* **48**, 39–43 (2017).

38. Labbe, R. FilterPy—Kalman filters and other optimal and non-optimal estimation filters in Python (2017); <https://github.com/rlabbe/filterpy>.
39. Rauch, H. E., Tung, F. & Striebel, C. T. Maximum likelihood estimates of linear dynamic systems. *AIAA J.* **3**, 1445–1450 (1965).
40. Winter, D. A. *Biomechanics and Motor Control of Human Movement* (Wiley, 2009).
41. Knott, G. D. *Interpolating Cubic Splines* (Birkhäuser, 2000).
42. Jayne, B. C. Muscular mechanisms of snake locomotion: an electromyographic study of lateral undulation of the Florida banded water snake (*Nerodia fasciata*) and the yellow rat snake (*Elaphe obsoleta*). *J. Morphol.* **197**, 159–181 (1988).
43. Gillis, G. B. Neuromuscular control of anguilliform locomotion: patterns of red and white muscle activity during swimming in the American eel *Anguilla rostrata*. *J. Exp. Biol.* **201**, 3245–3256 (1998).
44. Jafari, F., Ross, S. D., Vlachos, P. P. & Socha, J. J. A theoretical analysis of pitch stability during gliding in flying snakes. *Bioinspir. Biomim.* **9**, 025014 (2014).
45. Yeaton, I. J., Socha, J. J. & Ross, S. D. Global dynamics of non-equilibrium gliding in animals. *Bioinspir. Biomim.* **12**, 026013 (2017).
46. Haque, A. & Dickman, J. D. Vestibular gaze stabilization: different behavioral strategies for arboreal and terrestrial avians. *J. Neurophysiol.* **93**, 1165–1173 (2005).
47. Yamada, H., Mori, M. & Hirose, S. Stabilization of the head of an undulating snake-like robot. In *2007 IEEE/RSJ International Conference on Intelligent Robots and Systems*, 3566–3571 (IEEE, 2007).

### Acknowledgements

We thank the Virginia Tech Institute for Creativity, Arts, and Technology (ICAT) for facility access, crew support and funding. In particular, we thank T. Uptegrove, N. McGowan and B. Knapp. We thank G. Nave, T. Weiss, M. Graham, J. Whitehead and J. Garrett for assisting with the kinematics experiments. We thank H. Pendar for help with developing the mathematical model of snake flight, and F. Jafari for discussions about the role of undulation. We thank G. Nave, P. Nolan, K. Tetreault, N. Hall, F. Jafari and M. Graham for critical reading of early versions of the manuscript. We thank B. Robert, J. Settlege and A. Rizzo for help with IACUC. We also thank M. LaBarbera for his original suggestion that undulation might function as a mechanism of dynamic stability. This work was supported by the National Science Foundation under grant 1351322 to J.J.S., grants 1537349 and 1922516 to S.D.R. and grant 0966125 to S.D.R. and J.J.S.

### Author contributions

J.J.S. and I.J.Y. conceived the project, I.J.Y. and J.J.S. designed and conducted the experiments; I.J.Y. and S.D.R. developed the mathematical model; G.A.B. helped conduct experiments and export the experimental data; I.J.Y. analysed the experimental data, implemented the simulations, analysed the simulation output and produced all figures; I.J.Y., S.D.R. and J.J.S. wrote the manuscript.

### Competing interests

The authors declare no competing interests.

### Additional information

**Supplementary information** is available for this paper at <https://doi.org/10.1038/s41567-020-0935-4>.

**Correspondence and requests for materials** should be addressed to I.J.Y.

**Peer review information** *Nature Physics* thanks Daniel Goldman, Michael Shelley and the other, anonymous, reviewer(s) for their contribution to the peer review of this work.

**Reprints and permissions information** is available at [www.nature.com/reprints](http://www.nature.com/reprints).